

Bidirectional multi-photon communication between remote superconducting nodes

Joel Grebel,¹ Haoxiong Yan,¹ Ming-Han Chou,^{1,2} Gustav Andersson,¹ Christopher R. Conner,¹ Yash J. Joshi,¹ Jacob M. Miller,^{1,2} Rhys G. Povey,^{1,2} Hong Qiao,¹ Xuntao Wu,¹ and Andrew N. Cleland^{1,3}

¹*Pritzker School of Molecular Engineering, University of Chicago, Chicago IL 60637, USA*

²*Department of Physics, University of Chicago, Chicago IL 60637, USA*

³*Center for Molecular Engineering, Argonne National Laboratory, Lemont IL 60439, USA*

(Dated: October 3, 2023)

Quantum communication testbeds provide a useful resource for experimentally investigating a variety of communication protocols. Here we demonstrate a superconducting circuit testbed with bidirectional multi-photon state transfer capability using time-domain shaped wavepackets. The system we use to achieve this comprises two remote nodes, each including a tunable superconducting transmon qubit and a tunable microwave-frequency resonator, linked by a 2 m-long superconducting coplanar waveguide, which serves as a transmission line. We transfer both individual and superposition Fock states between the two remote nodes, and additionally show that this bidirectional state transfer can be done simultaneously, as well as used to entangle elements in the two nodes.

Long range, high fidelity communication of quantum information has applications in several areas [1], including secure communication using quantum key cryptography [2], as well as serving as the backbone for a future quantum internet [3]. These applications require sources of entangled photons, preferably on-demand, to perform most quantum cryptographic functions. Photons at optical frequencies are a natural choice for the communication medium, due to their high energies compared to ambient thermal energies, low propagation loss at room temperature, and widely available fiber communication technology. However, high fidelity and high rate sources of on-demand entangled photons are still lacking at optical frequencies, yielding to date low information transfer rates [4–8]. At microwave frequencies, superconducting circuits provide a flexible platform for designing high fidelity control of computational elements with reasonably low-loss memory elements, and can deterministically generate microwave photons entangled with qubits. Combined with variable superconducting couplers, these elements can be used to experimentally test long-range communication protocols [9] with itinerant photon wavepackets [10–19], as well as modular quantum computing approaches, using the standing modes in a weakly-coupled communication waveguide [20–23]. Several experiments using superconducting circuits have demonstrated deterministic transfer of both single [14–16] and multi-photon states [17] between remote nodes, using time-symmetric shaped wavepackets to improve transfer fidelity [24]. However, with the exception of Ref. 16 and 19, these all involved the use of lossy microwave circulators, thus only supporting communication in one direction.

Here we demonstrate bidirectional, multi-photon state transfer with shaped wavepackets between two remote superconducting qubit nodes, eliminating the microwave circulators used in earlier experiments [14, 15, 17]. Circulators are useful for preventing unwanted reflections from emitted signals, simplifying tune-up and operation

of these circuits. However, existing broadband commercial circulators cannot reverse their polarity *in situ*, and further are a significant source of loss; while broadband parametric circulators may overcome these limitations [25, 26], these are not yet available. Here we implement itinerant bidirectional communication, where itinerant means the pulsed signals have time-domain envelopes shorter than the length of the transmission line; we achieve this by using fast dynamic couplers at each node, allowing us to complete signal transfers with low reflection rates and sufficient speed that interference between emission and reflection signals can be avoided [16].

The experimental device is shown in Fig. 1. Each of the two nodes comprises a frequency-tunable superconducting Xmon qubit [27] $Q1$ ($Q2$), capacitively-coupled to a frequency-tunable resonator $R1$ ($R2$), which is in turn connected via a variable coupler [28] to one end of a 2 m-long, $50\ \Omega$ coplanar waveguide. The tunable resonators are implemented as a resonant section of coplanar waveguide terminated by a superconducting quantum interference device (SQUID) [29], connected to ground through the variable coupler. Control flux lines allow tuning the resonator over a range of 1.5 GHz, limited in the experiment to 0.5 GHz by the control electronics. The variable couplers afford control of the coupling strength of the resonator to the 2-m long transmission line, where the resonator decay rate $\kappa_r/2\pi$ into the transmission line can be varied dynamically from 0-55 MHz, with control signals as short as 3 ns, limited by control-line filtering. The transmission line itself is a $50\ \Omega$ coplanar waveguide, galvanically connected to each variable coupler. All components are fabricated on a single $2\text{ cm} \times 2\text{ cm}$ sapphire die, shown in a back-lit optical micrograph in Fig. 1(b). Fabrication details are provided in Ref. 30. The device was wirebonded to a copper printed circuit board that was in turn placed in an aluminum enclosure, the latter placed in a double magnetic shield mounted to the 10 mK mixing chamber of a dilution refrigerator. A wiring diagram showing the cabling for the dilution refrigerator,

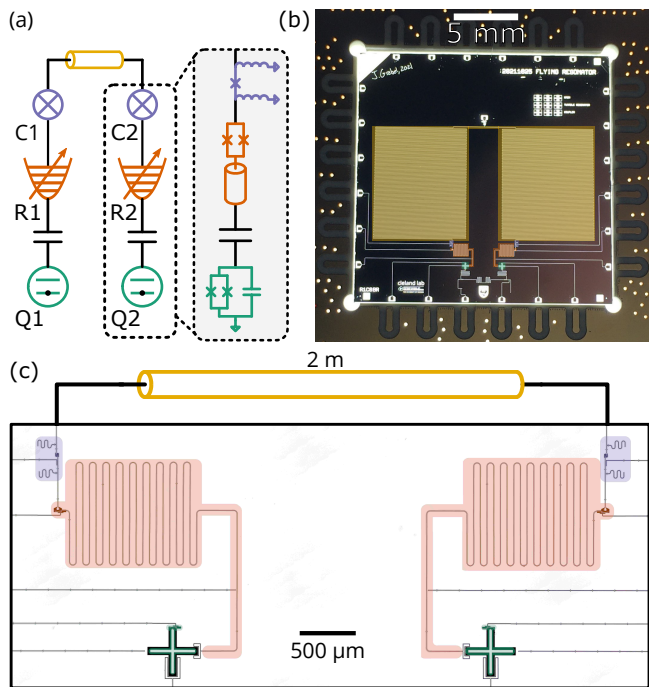


FIG. 1. Experimental layout. (a) Block diagram for the experiment, comprising two tunable qubits $Q1$, $Q2$ (green), capacitively-coupled to two tunable resonators $R1$, $R2$ (orange), in turned coupled via two variable couplers $C1$, $C2$ (purple) to a 2 m-long waveguide (yellow). Circuit representations of these elements are shown in the dashed box. (b) Backside-illuminated optical photograph of fabricated device with false coloring, showing all components including the 2 m-long coplanar waveguide, as well as the printed circuit board to which the die is wirebonded for signal routing. (c) Optical micrograph of device with false coloring corresponding to components shown in panel (a). The coplanar waveguide is patterned on the same die but is cropped from this image; see panel (b).

and a schematic for the control and readout circuitry, is shown in the supplemental material [30].

Standard characterization of the qubits yields characteristic lifetimes $T_{1,Q1} = 20 \mu\text{s}$ and $T_{1,Q2} = 22 \mu\text{s}$ at the qubit operating frequencies of $f_{Q1} = 4.57 \text{ GHz}$ and $f_{Q2} = 4.5 \text{ GHz}$. The qubit Ramsey lifetimes T_2 at the same operating frequencies are $2.6 \mu\text{s}$ and $0.56 \mu\text{s}$, respectively.

To characterize the tunable resonators, we swap single excitations from the qubits to their respective resonators by tuning the excited qubit into resonance with the resonator for a calibrated time, with the variable couplers turned off. Using the qubits to monitor the subsequent resonator decay, we measure characteristic T_1 and T_2 times of $T_{1,R1} = 4.57 \mu\text{s}$, $T_{1,R2} = 0.86 \mu\text{s}$, $T_{2,R1} = 0.95 \mu\text{s}$, and $T_{2,R2} = 0.9 \mu\text{s}$. All qubit-resonator swaps are measured at frequency $f_R = 4.058 \text{ GHz}$ with qubit-resonator coupling strength $g_{QR}/2\pi = 6.8 \text{ MHz}$ set by the geometric capacitance $C = 1.4 \text{ fF}$ connecting these elements.

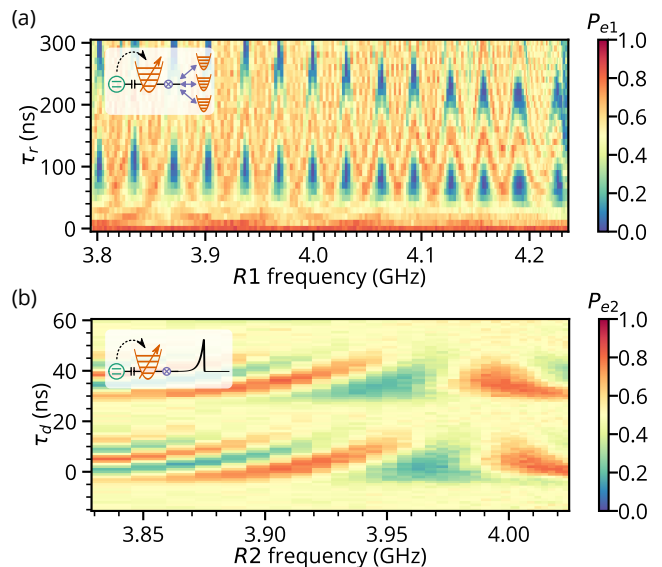


FIG. 2. (a) Standing waveguide modes seen by $R1$ at weak coupling. After a single excitation is swapped into $R1$, the coupling to the waveguide is turned on for time τ_r while tuning the resonator frequency. (b) Ramsey-like experiment showing itinerant emission and recapture of a $|0\rangle + |1\rangle$ state in $R2$. The superposition state is swapped from $Q2$ to $R2$, emitted and recaptured from $R2$ with 20 ns rectangular pulses separated by delay τ_d while tuning the resonator frequency, swapped back to $Q2$, and a $\pi/2$ pulse is applied to $Q2$ before measurement.

We characterize the transmission waveguide by swapping excitations into individual standing waveguide modes as shown in Fig. 2(a), at weak coupling $g_{RW} \ll \omega_{FSR}$, with $g_{RW}/2\pi < 3.4 \text{ MHz}$ the resonator/waveguide coupling strength, and $\omega_{FSR}/2\pi = 31 \text{ MHz}$ the waveguide free spectral range. The waveguide T_1 coherence times are in the range of $4 - 5 \mu\text{s}$. At stronger coupling, we emit itinerant wavepackets into the waveguide, which requires coupling to a number of adjacent waveguide modes. Figure 2(b) shows a Ramsey-like experiment with $\pi/2$ pulses on $Q2$ at the beginning and end of the pulse sequence, where we emit and then recapture a superposition $|0\rangle + |1\rangle$ state in $R2$ for different resonator frequencies. The return time for the pulses is independent of the resonator frequency in this regime; fringes at different frequencies indicate phase coherence in the waveguide. See Ref. 30 for more characterization details.

We prepare Fock states in each tunable resonator by exciting the adjacent qubit, then resonantly swapping photons one at a time into the resonator [31]. In Fig. 3(a) and (b), we swap an $n = 1$ Fock state between the resonators via the communication waveguide, by first exciting either resonator via its adjacent qubit with both resonators tuned to f_R , and controlling the variable couplers with calibrated pulses to perform an itinerant release-and-catch transfer of the excitation [16]. We then swap

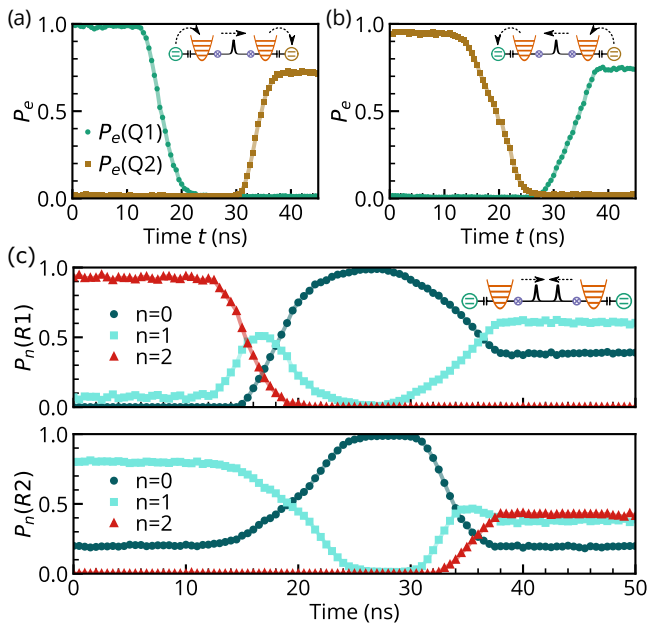


FIG. 3. Transfer of excited qubit states, from (a) qubit $Q1$ to qubit $Q2$ and (b) $Q2$ to $Q1$. We excite the emitting qubit, swap the excitation to the adjacent resonator, transmit the excitation as a wavepacket to the distant resonator by time-varying control of the couplers between the resonators and waveguide, then finally swap to the receiving qubit. Lines are a guide for the eye. (c) Simultaneous state swaps between the resonators. We initialize resonator $R1$ in a 2-photon Fock state while initializing resonator $R2$ in a 1-photon Fock state. These states are simultaneously released into the transmission line as itinerant wavepackets that are then captured by the receiving resonators, and we use the associated qubit to analyze its associated resonator's final state. The population of each resonator's Fock states $|F_n\rangle$, $n = 0, 1, 2$ is shown as a function of time.

the receiving resonator's excitation to the corresponding qubit for measurement. We release and subsequently capture the wavepacket by dynamically tuning the coupling strength for each coupler, and optimize the state transfer using Bayesian optimization [32]. During this process, we hold each resonator's frequency constant by applying a stabilizing flux pulse to its SQUID; this corrects both for frequency changes due to the changing loading electrical circuit as well as flux cross-talk. We transfer single photons in either direction, with an efficiency of 0.72 for $Q1 \rightarrow Q2$ transfers, and an efficiency of 0.74 for the reverse direction. Here efficiency is defined as $\mathcal{E} = \langle P_j \rangle / \langle P_i \rangle$, where $P_{i,j}$ are the release and capture qubit populations, respectively. The inefficiency is likely dominated by non-ideal pulse shaping and timing, as the inverse loss rate in the system is well-characterized and significantly longer than the transfer time.

To demonstrate bidirectional itinerant state transfer, we prepare dual resonator states using the adjacent qubits and then simultaneously release these into the

communication waveguide, using the qubits to monitor the resonator populations. In Fig. 3(c) we show the schematic process, where we prepare resonator $R1$ with a two-photon Fock state while preparing resonator $R2$ with a one-photon Fock state. We then use both variable couplers to perform a simultaneous itinerant release-and-catch of photons transmitted in each direction in the communication waveguide. To reconstruct the resulting population in the resonators, we resonantly interact the resonator with its corresponding qubit for a variable length of time, monitoring the qubit excited state probability. We then fit the time-dependent response to a model Hamiltonian for the combined system [33]. The reconstructed resonator Fock state probabilities for Fock states $n = 0, 1, 2$ are shown in Fig. 3 as a function of time. Due to the use of slightly different control pulses, in this experiment the resonator one-photon transfer efficiency is 0.82, while the two-photon transfer efficiency is 0.64.

We can also use this system to generate and transfer more complex quantum states. In Fig. 4(a), we show the preparation and transfer of superposition Fock states. We prepare the $|0\rangle + |1\rangle$ superposition states in resonator $R1$ by swapping a $|g\rangle + |e\rangle$ state from qubit $Q1$, achieving a state fidelity $\mathcal{F} = 0.99(6)$. We perform an itinerant state transfer via the communication channel to resonator $R2$ with fidelity $\mathcal{F} = 0.94(0)$, where $\mathcal{F}(\rho, \sigma) = \text{tr} \sqrt{\rho^{1/2} \sigma \rho^{1/2}}$ of the measured density matrix ρ to the ideal state σ . In a similar fashion, we prepare the $|0\rangle + |2\rangle$ superposition in $R2$ by exciting $Q1$ to the $|g\rangle + |f\rangle$ state with two subsequent swaps to $R1$, achieving a fidelity $\mathcal{F} = 0.95(2)$. The $|0\rangle + |2\rangle$ superposition is then transferred by wavepacket via the communication channel to $R1$, with fidelity $\mathcal{F} = 0.82(3)$. The Wigner tomograms in the figure are reconstructed by using convex optimization to find the most likely state that fits the Fock distribution as a function of displacement [34, 35]. To measure the final resonator Fock state distribution, we tune the qubit, initially in its ground state, to the resonator frequency, and fit the subsequent qubit oscillations to a model system [30, 33]. The phase difference between the prepared and received states are possibly due to the resonator frequency varying slightly during wavepacket release and capture, due to non-ideal control pulses. Wigner tomograms of the raw parity data are given in [30].

To demonstrate the generation of remote entanglement in this system, shown in Fig. 4 (b), we create NOON states, superposition states in which N -photon states in one resonator are superposed with vacuum states in the other resonator, in the form $|\psi\rangle = \frac{1}{\sqrt{2}}(|N0\rangle - |0N\rangle)$. In Fig. 4 (b), for the $N = 1$ NOON state, we prepare a one-photon Fock state in $R1$, then, via an itinerant transfer, move half the population to $R2$. We then measure the joint resonator state with bipartite Wigner tomography [36], using convex optimization to find the most likely

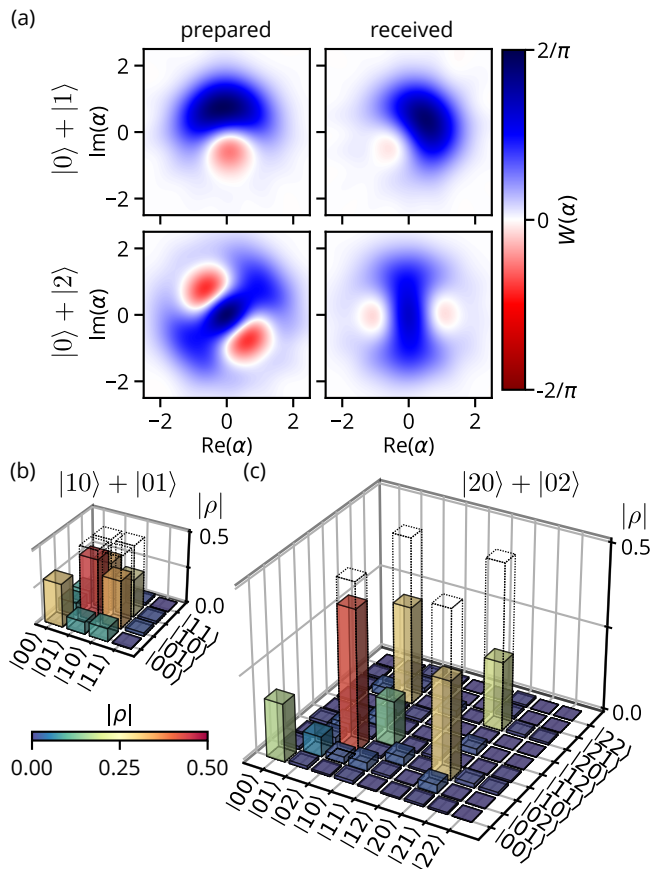


FIG. 4. (a) Transfer of superposition Fock states. We prepare $|0\rangle + |1\rangle$ and $|0\rangle + |2\rangle$ states in resonator $R1$ and transfer these as itinerant wavepackets to resonator $R2$. We use the corresponding qubits to reconstruct the Wigner tomograms in both resonators, as described in the main text. NOON states $|n0\rangle + |0n\rangle$ with (b) $n = 1$ and (c) $n = 2$ itinerant transfers between the two tunable resonators. State preparation is described in the main text. Dotted lines indicate the ideal NOON states while transparent colored bars are the reconstructed density matrices.

state given by the joint resonator Fock distribution as a function of displaced resonator states [34, 35]. Similar to the single resonator case, we measure the joint resonator Fock distribution by tuning both qubits, initially in their ground states, into resonance with their respective resonators, then fit the resulting qubit population oscillations to a model system [30, 36]. The fidelity of the prepared state is found to be $\mathcal{F} = 0.82(7)$. In Fig. 4 (c), for the $N = 2$ NOON state, we first prepare a one-excitation Bell state $(|eg\rangle - |ge\rangle)/\sqrt{2}$ in the two qubits, by swapping half an excitation from $Q1$ to $R1$, followed by an itinerant transfer from $R1$ to $R2$, and finally swapping the half-excitation to $Q2$. We next excite the $e - f$ transition in each qubit, resulting in the state $(|fg\rangle - |gf\rangle)/\sqrt{2}$, then transfer the qubit populations to the resonators with two subsequent swaps, resulting in

the final resonator state $(|20\rangle - |02\rangle)/\sqrt{2}$. The fidelity to the ideal state is $\mathcal{F} = 0.78(0)$. Fig. 4 (b) and (c) show the reconstructed absolute value of the density matrices for the two states. The major sources of infidelity are photon loss during the transfer process and while stored in the resonators.

In conclusion, we demonstrate multi-photon bidirectional communication between two quantum-coherent superconducting nodes coupled by a 2 m-long coplanar waveguide, with states sent using itinerant photons whose pulse lengths of 0.45 ns are significantly less than the 2 ns length of the waveguide. Future experiments might transfer multi-photon qubits such as the cat [37] or GKP [38] encoding states between resonators in the testbed. Other communication protocols might be achieved by dynamically varying both the resonator frequencies and the coupling strength of each resonator to the waveguide during wavepacket emission and capture. We can judge the relative performance of different communication protocols using a single system, e.g. using final state fidelities. Tens of individual waveguide modes can be addressed by each node; this system thus has further potential as a quantum random access memory [39]. Additional nodes may be connected to the network by adding multiple coupled waveguides to each resonator, with nodes in separate modules if needed [22]. The most significant limitations in this system are the challenges in the time-domain control of both the couplers and resonators, which has to account for circuit loading, flux cross-talk and cable-related pulse distortions. Higher fidelities might be achieved using machine learning techniques such as implemented in Ref. [40, 41]; more precise pulse control with faster electronics and fewer control wiring filters; and a longer waveguide that allows longer duration itinerant photon pulse shapes, making time-domain control less challenging.

ACKNOWLEDGMENTS

We thank P. J. Duda for helpful discussions and W. D. Oliver and G. Calusine at Lincoln Laboratories for the provision of a traveling-wave parametric amplifier. Financial support was provided by the NSF QLCI for HQAN (NSF Award 2016136), the U.S. Department of Energy Office of Science National Quantum Information Science Research Centers, the Army Research Office-Laboratory for Physical Sciences (contract W911NF-23-1-0077), and the University of Chicago MRSEC (NSF award DMR-2011854). We made use of the Pritzker Nanofabrication Facility, partially supported by SHyNE, a node of the National Science Foundations National Nanotechnology Coordinated Infrastructure (NSF Grant No. NNCI ECCS-2025633). A.N.C. was supported in part by the DOE, Office of Basic Energy Sciences. The authors declare no competing financial interests. Corre-

spondence and requests for materials should be addressed to A. N. Cleland (anc@uchicago.edu).

J.G. designed and fabricated the devices, performed the experiment and analyzed the data. H.Y., M.H.C., and G.A. provided suggestions for measurement and data analysis. A.N.C. advised on all efforts. All authors contributed to discussion and production of the manuscript.

-
- [1] N. Gisin and R. Thew, Quantum communication, *Nature Photonics* **1**, 165 (2007).
- [2] A. K. Ekert, Quantum cryptography based on Bell's theorem, *Phys. Rev. Lett.* **67**, 661 (1991).
- [3] H. J. Kimble, The quantum internet, *Nature* **453**, 1023 (2008).
- [4] A. Reiserer, Colloquium: Cavity-enhanced quantum network nodes, *Rev. Mod. Phys.* **94**, 041003 (2022).
- [5] H.-J. Briegel, W. Dür, J. I. Cirac, and P. Zoller, Quantum repeaters: The role of imperfect local operations in quantum communication, *Phys. Rev. Lett.* **81**, 5932 (1998).
- [6] W. J. Munro, K. Azuma, K. Tamaki, and K. Nemoto, Inside quantum repeaters, *IEEE Journal of Selected Topics in Quantum Electronics* **21**, 78 (2015).
- [7] J. Yin, Y. Cao, Y.-H. Li, S.-K. Liao, L. Zhang, J.-G. Ren, W.-Q. Cai, W.-Y. Liu, B. Li, H. Dai, G.-B. Li, Q.-M. Lu, Y.-H. Gong, Y. Xu, S.-L. Li, F.-Z. Li, Y.-Y. Yin, Z.-Q. Jiang, M. Li, J.-J. Jia, G. Ren, D. He, Y.-L. Zhou, X.-X. Zhang, N. Wang, X. Chang, Z.-C. Zhu, N.-L. Liu, Y.-A. Chen, C.-Y. Lu, R. Shu, C.-Z. Peng, J.-Y. Wang, and J.-W. Pan, Satellite-based entanglement distribution over 1200 kilometers, *Science* **356**, 1140 (2017), <https://www.science.org/doi/pdf/10.1126/science.aan3211>.
- [8] D. Du, P. Stankus, O.-P. Saira, M. Flament, S. Sagona-Stophel, M. Namazi, D. Katramatos, and E. Figueroa, An elementary 158 km long quantum network connecting room temperature quantum memories, *arXiv preprint arXiv:2101.12742* (2021).
- [9] M. Casariego, E. Z. Cruzeiro, S. Gherardini, T. Gonzalez-Raya, R. Andr, G. Frazo, G. Catto, M. Mtnen, D. Datta, K. Viisanen, J. Govenius, M. Prunnila, K. Tuominen, M. Reichert, M. Renger, K. G. Fedorov, F. Deppe, H. van der Vliet, A. J. Matthews, Y. Fernandez, R. Assouly, R. Dassonneville, B. Huard, M. Sanz, and Y. Omar, Propagating quantum microwaves: towards applications in communication and sensing, *Quantum Science and Technology* **8**, 023001 (2023).
- [10] Y. Yin, Y. Chen, D. Sank, P. J. J. O'Malley, T. C. White, R. Barends, J. Kelly, E. Lucero, M. Mariantoni, A. Megrant, C. Neill, A. Vainsencher, J. Wenner, A. N. Korotkov, A. N. Cleland, and J. M. Martinis, Catch and release of microwave photon states, *Phys. Rev. Lett.* **110**, 107001 (2013).
- [11] J. Wenner, Y. Yin, Y. Chen, R. Barends, B. Chiaro, E. Jeffrey, J. Kelly, A. Megrant, J. Y. Mutus, C. Neill, P. J. J. O'Malley, P. Roushan, D. Sank, A. Vainsencher, T. C. White, A. N. Korotkov, A. N. Cleland, and J. M. Martinis, Catching time-reversed microwave coherent state photons with 99.4% absorption efficiency, *Phys. Rev. Lett.* **112**, 210501 (2014).
- [12] M. Pierre, I.-M. Svensson, S. Raman Sathyamoorthy, G. Johansson, and P. Delsing, Storage and on-demand release of microwaves using superconducting resonators with tunable coupling, *Appl. Phys. Lett.* **104**, 232604 (2014).
- [13] S. J. Srinivasan, N. M. Sundaresan, D. Sadri, Y. Liu, J. M. Gambetta, T. Yu, S. M. Girvin, and A. A. Houck, Time-reversal symmetrization of spontaneous emission for quantum state transfer, *Phys. Rev. A* **89**, 033857 (2014).
- [14] P. Kurpiers, P. Magnard, T. Walter, B. Royer, M. Pechal, J. Heinsoo, Y. Salath, A. Akin, S. Storz, J.-C. Besse, S. Gasparinetti, A. Blais, and A. Wallraff, Deterministic quantum state transfer and remote entanglement using microwave photons, *Nature* **558**, 264 (2018).
- [15] P. Campagne-Ibarcq, E. Zalys-Geller, A. Narla, S. Shankar, P. Reinhold, L. Burkhardt, C. Axline, W. Pfaff, L. Frunzio, R. J. Schoelkopf, and M. H. Devoret, Deterministic remote entanglement of superconducting circuits through microwave two-photon transitions, *Phys. Rev. Lett.* **120**, 200501 (2018).
- [16] Y. P. Zhong, H.-S. Chang, K. J. Satzinger, M.-H. Chou, A. Bienfait, C. R. Conner, . Dumur, J. Grebel, G. A. Peairs, R. G. Povey, D. I. Schuster, and A. N. Cleland, Violating bells inequality with remotely connected superconducting qubits, *Nature Physics* **15**, 741 (2019).
- [17] C. J. Axline, L. D. Burkhardt, W. Pfaff, M. Zhang, K. Chou, P. Campagne-Ibarcq, P. Reinhold, L. Frunzio, S. M. Girvin, L. Jiang, M. H. Devoret, and R. J. Schoelkopf, On-demand quantum state transfer and entanglement between remote microwave cavity memories, *Nature Physics* **14**, 705 (2018).
- [18] P. Magnard, S. Storz, P. Kurpiers, J. Schär, F. Marxer, J. Lütolf, T. Walter, J.-C. Besse, M. Gabureac, K. Reuer, A. Akin, B. Royer, A. Blais, and A. Wallraff, Microwave quantum link between superconducting circuits housed in spatially separated cryogenic systems, *Phys. Rev. Lett.* **125**, 260502 (2020).
- [19] J. Qiu, Y. Liu, J. Niu, L. Hu, Y. Wu, L. Zhang, W. Huang, Y. Chen, J. Li, S. Liu, *et al.*, Deterministic quantum teleportation between distant superconducting chips, *arXiv preprint arXiv:2302.08756* (2023).
- [20] H.-S. Chang, Y. P. Zhong, A. Bienfait, M.-H. Chou, C. R. Conner, E. Dumur, J. Grebel, G. A. Peairs, R. G. Povey, K. J. Satzinger, and A. N. Cleland, Remote entanglement via adiabatic passage using a tunably dissipative quantum communication system, *Phys. Rev. Lett.* **124**, 240502 (2020).
- [21] L. D. Burkhardt, J. D. Teoh, Y. Zhang, C. J. Axline, L. Frunzio, M. H. Devoret, L. Jiang, S. M. Girvin, and R. J. Schoelkopf, Error-detected state transfer and entanglement in a superconducting quantum network, *PRX Quantum* **2**, 030321 (2021).
- [22] Y. Zhong, H.-S. Chang, A. Bienfait, t. Dumur, M.-H. Chou, C. R. Conner, J. Grebel, R. G. Povey, H. Yan, D. I. Schuster, and A. N. Cleland, Deterministic multi-qubit entanglement in a quantum network, *Nature* **590**, 571 (2021).
- [23] J. Niu, L. Zhang, Y. Liu, J. Qiu, W. Huang, J. Huang, H. Jia, J. Liu, Z. Tao, W. Wei, Y. Zhou, W. Zou, Y. Chen, X. Deng, X. Deng, C. Hu, L. Hu, J. Li, D. Tan, Y. Xu, F. Yan, T. Yan, S. Liu, Y. Zhong, A. N. Cleland, and D. Yu, Low-loss interconnects for modular superconducting quantum processors, *Nature Electronics* **6**, 235

- (2023).
- [24] J. I. Cirac, P. Zoller, H. J. Kimble, and H. Mabuchi, Quantum state transfer and entanglement distribution among distant nodes in a quantum network, *Phys. Rev. Lett.* **78**, 3221 (1997).
- [25] M. Beck, M. Selvanayagam, A. Carniol, S. Cairns, and C. Mancini, Wideband Josephson parametric isolator, arXiv preprint arXiv:2212.08563 (2022).
- [26] R. Kwende, T. White, and O. Naaman, Josephson parametric circulator with same-frequency signal ports, 200 mhz bandwidth, and high dynamic range, *Appl. Phys. Lett.* **122**, 224001 (2023).
- [27] R. Barends, J. Kelly, A. Megrant, D. Sank, E. Jeffrey, Y. Chen, Y. Yin, B. Chiaro, J. Mutus, C. Neill, P. O'Malley, P. Roushan, J. Wenner, T. C. White, A. N. Cleland, and J. M. Martinis, Coherent Josephson qubit suitable for scalable quantum integrated circuits, *Phys. Rev. Lett.* **111**, 080502 (2013).
- [28] Y. Chen, C. Neill, P. Roushan, N. Leung, M. Fang, R. Barends, J. Kelly, B. Campbell, Z. Chen, B. Chiaro, A. Dunsworth, E. Jeffrey, A. Megrant, J. Y. Mutus, P. J. J. O'Malley, C. M. Quintana, D. Sank, A. Vainsencher, J. Wenner, T. C. White, M. R. Geller, A. N. Cleland, and J. M. Martinis, Qubit architecture with high coherence and fast tunable coupling, *Phys. Rev. Lett.* **113**, 220502 (2014).
- [29] M. Sandberg, C. M. Wilson, F. Persson, T. Bauch, G. Johansson, V. Shumeiko, T. Duty, and P. Delsing, Tuning the field in a microwave resonator faster than the photon lifetime, *Appl. Phys. Lett.* **92**, 203501 (2008).
- [30] See Supplemental Material for details on experimental setup, numerical analysis, and device tuneup.
- [31] M. Hofheinz, E. M. Weig, M. Ansmann, R. C. Bialczak, E. Lucero, M. Neeley, A. D. O'Connell, H. Wang, J. M. Martinis, and A. N. Cleland, Generation of Fock states in a superconducting quantum circuit, *Nature* **454**, 310 (2008).
- [32] F. Nogueira, Bayesian Optimization: Open source constrained global optimization tool for Python (2014–).
- [33] M. Hofheinz, H. Wang, M. Ansmann, R. C. Bialczak, E. Lucero, M. Neeley, A. D. O'Connell, D. Sank, J. Wenner, J. M. Martinis, and A. N. Cleland, Synthesizing arbitrary quantum states in a superconducting resonator, *Nature* **459**, 546 (2009).
- [34] M. Grant and S. Boyd, CVX: Matlab software for disciplined convex programming, version 2.1, <http://cvxr.com/cvx> (2014).
- [35] I. Strandberg, Simple, reliable, and noise-resilient continuous-variable quantum state tomography with convex optimization, *Phys. Rev. Appl.* **18**, 044041 (2022).
- [36] H. Wang, M. Mariani, R. C. Bialczak, M. Lenander, E. Lucero, M. Neeley, A. D. O'Connell, D. Sank, M. Weides, J. Wenner, T. Yamamoto, Y. Yin, J. Zhao, J. M. Martinis, and A. N. Cleland, Deterministic entanglement of photons in two superconducting microwave resonators, *Phys. Rev. Lett.* **106**, 060401 (2011).
- [37] R. Lescanne, M. Villiers, T. Peronnin, A. Sarlette, M. Delbecq, B. Huard, T. Kontos, M. Mirrahimi, and Z. Leghtas, Exponential suppression of bit-flips in a qubit encoded in an oscillator, *Nature Physics* **16**, 509 (2020).
- [38] P. Campagne-Ibarcq, A. Eickbusch, S. Touzard, E. Zalys-Geller, N. E. Frattini, V. V. Sivak, P. Reinhold, S. Puri, S. Shankar, R. J. Schoelkopf, L. Frunzio, M. Mirrahimi, and M. H. Devoret, Quantum error correction of a qubit encoded in grid states of an oscillator, *Nature* **584**, 368 (2020).
- [39] C. T. Hann, C.-L. Zou, Y. Zhang, Y. Chu, R. J. Schoelkopf, S. M. Girvin, and L. Jiang, Hardware-efficient quantum random access memory with hybrid quantum acoustic systems, *Phys. Rev. Lett.* **123**, 250501 (2019).
- [40] V. V. Sivak, A. Eickbusch, H. Liu, B. Royer, I. Tsioutsios, and M. H. Devoret, Model-free quantum control with reinforcement learning, *Phys. Rev. X* **12**, 011059 (2022).
- [41] X. Wu et al. In preparation, .

Supplemental Material for “Bidirectional multi-photon communication between remote superconducting nodes”

J. Grebel,¹ G. Andersson,¹ M.-H. Chou,^{1,2} C. R. Conner,¹ Y. J. Joshi,¹ J. M. Miller,^{1,2} R. G. Povey,^{1,2} H. Qiao,¹ X. Wu,¹ H. Yan,¹ and A. N. Cleland^{1,3}

¹*Pritzker School of Molecular Engineering, University of Chicago, Chicago IL 60637, USA*

²*Department of Physics, University of Chicago, Chicago IL 60637, USA*

³*Center for Molecular Engineering, Argonne National Laboratory, Lemont IL 60439, USA*

(Dated: October 3, 2023)

DEVICE FABRICATION AND WIRING

Fabrication

After depositing 100 nm of Al by electron beam evaporation on a sapphire substrate [1, 2], the qubits, resonators, and waveguide are patterned with photolithography and etched with a $\text{BCl}_3/\text{Cl}_2/\text{Ar}$ inductively coupled plasma (ICP). We locate any unwanted waveguide shorts both electrically with an on-chip probe and visually with a microscope. We then etch away these shorts with a targeted second photolithography process of the base layer and Cl etch. For the airbridge sacrificial layer, 200 nm of SiO_2 is electron beam evaporated on patterned photoresist followed by a N-methyl-2-pyrrolidone (NMP) liftoff at 80 °C. We deposit Josephson junctions with a Dolan bridge process using a PMMA/MAA bilayer patterned with electron beam lithography, aligned on the wafer using photolithographically defined markers (10 nm Ti, 150 nm Au). A final photolithography process defines both Josephson junction bandages and the top airbridge layer; following which the sample is Ar-ion milled and 200 nm of Al deposited with electron beam evaporation. After dicing individual device dies, we remove the sacrificial SiO_2 with vapor HF to form suspended airbridges [3]. More detailed fabrication information can be found in Ref. [4].

Resonant package modes

All components are fabricated on a single 2×2 cm sapphire substrate. The unusually large die size is needed to fit the entire transmission line. Unfortunately, at this die size, the box modes of both the die and package are near experimentally relevant frequencies with the frequencies f_{nml} given by [5]

$$f_{nml} = \frac{c}{2\pi\sqrt{\mu_r\epsilon_r}} \sqrt{\left(\frac{n\pi}{a}\right)^2 + \left(\frac{m\pi}{b}\right)^2 + \left(\frac{l\pi}{d}\right)^2}, \quad (\text{S1})$$

where n, m , and l are the mode numbers for the transverse electric (TE) and transverse magnetic (TM) modes in a rectangular cavity, with two out of three indices non-zero. The relative permeability and permittivity are given as μ_r and ϵ_r , c is the speed of light and a, b , and d are the cavity dimensions (for example along the Cartesian x, y, z directions).

For a 20 mm square sapphire die with $\epsilon_r = 11.4$, the lowest frequency mode is $f_{110,chip} = 3.14$ GHz, while using $\epsilon_r = 1$ and 27 mm square for the package mode gives $f_{110,package} = 7.85$ GHz. From this rough calculation, the die modes are within our typical superconducting circuit operating frequencies of 4-8 GHz while the package modes are above our operating frequencies. We tune the frequencies of our qubits and resonators to avoid these modes.

Wiring

A wiring diagram of the experiment is shown in Fig. S1. The qubit readout signals are connected to a TWPA obtained from Lincoln Laboratories with an input noise temperature measured in our lab of around 500 mK. Two microwave circulators are placed in front of the TWPA to prevent the qubit from being exposed to the TWPA pump and backwards amplified noise [6].

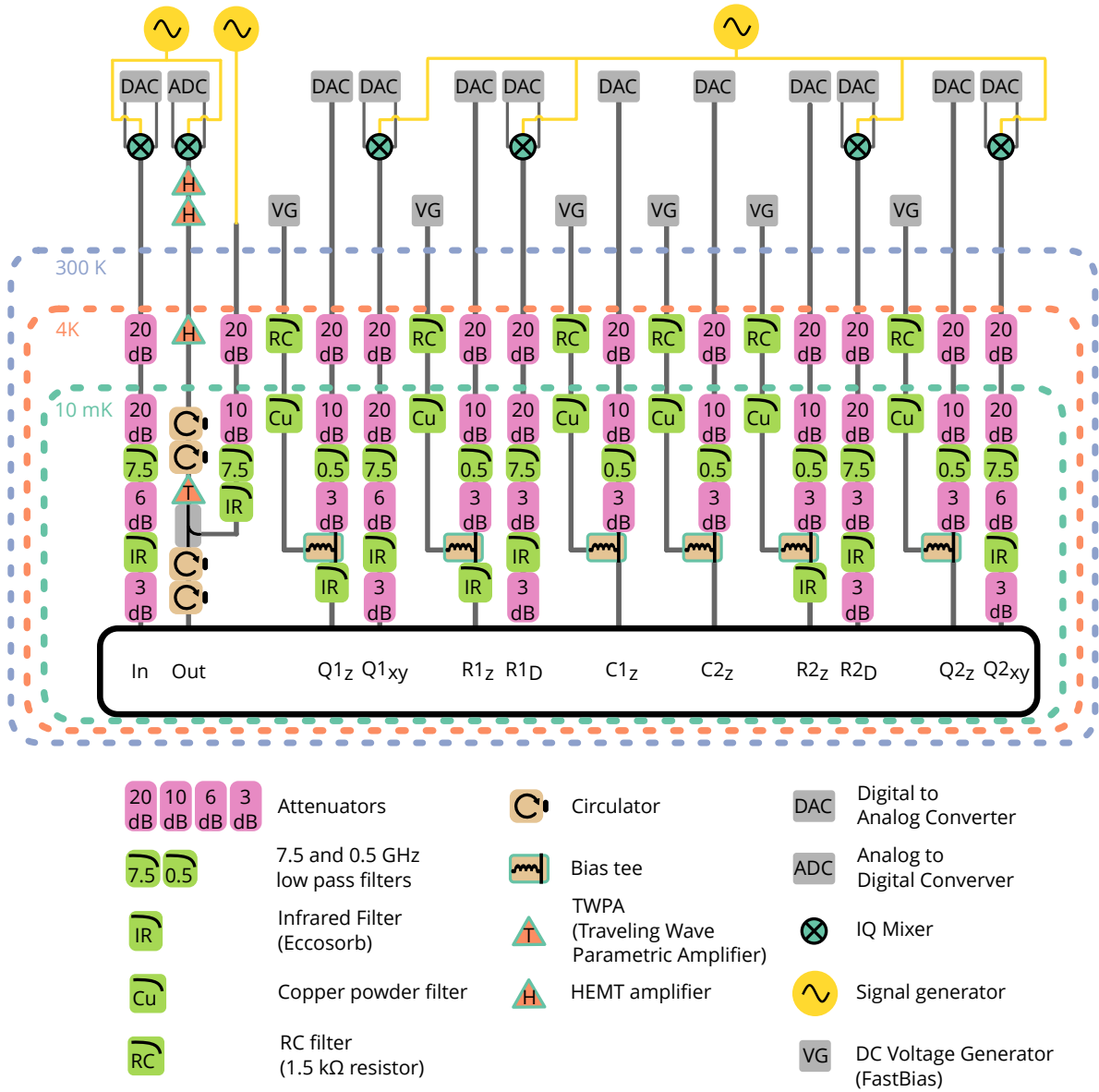


FIG. S1. Wiring diagram showing room temperature electronics, attenuators, and amplifiers. Input and output lines are used for qubit state readout. Qubits (Q) and resonators (R) have microwave (XY , D) lines and current bias (Z) lines, with the Z line combined with a low noise continuous bias current component and fast-bias components through a bias tee. Variable couplers only have a current bias line. Microwave signals are generated at room temperature using continuous signal generators that are then modulated by IQ mixers controlled by DACs. Microwave drive lines (In, XY , and D) are attenuated to reduce thermal noise. Low-noise voltage generators at room temperature are used as current sources by passing signals through a 1.5 kΩ resistor.

DEVICE MODELS

Resonator anharmonicity

Our resonator state preparation, readout and transfer protocols assume low resonator anharmonicity α_r . We estimate α_r by modeling the nonlinear correction due to a SQUID on one end of a waveguide resonator [7] with a small capacitance to ground on the other end. For a given eigenmode n of a waveguide resonator of length ℓ we vary the resonator's frequency ω_n within the range $(\pi v/\ell)n \leq \omega_n \leq (\pi v/\ell)(n + 1/2)$ by applying a flux through the boundary SQUID which changes its effective inductance. The lower and upper limits correspond to the resonance

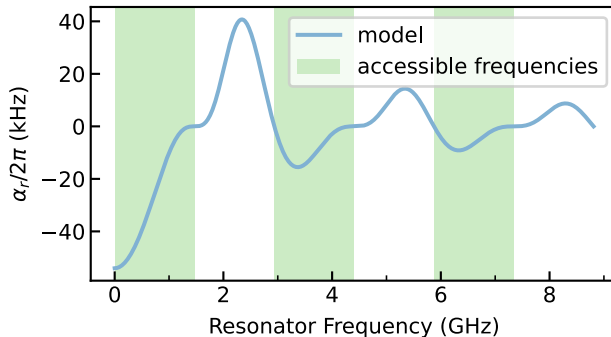


FIG. S2. Model for tunable resonator anharmonicity $\alpha_r/2\pi$ using Eq. S7 for a resonator of fixed length $\ell = 20.5$ mm for a 2:1 center:gap CPW on sapphire (see text). The tunable frequency range for the three lowest resonator modes are highlighted in green.

frequencies for a $\lambda/2$ and $\lambda/4$ resonator respectively. Here $v = c/\sqrt{\epsilon_{\text{eff}}}$ is the transmission line wave velocity, c is the speed of light in vacuum, and ϵ_{eff} is the effective dielectric constant for the transmission line. For a coplanar waveguide (CPW) on sapphire in vacuum, $\epsilon_{\text{eff}} \approx (1 + \epsilon_r)/2$ where the sapphire substrate has dielectric constant ϵ_r .

Assuming a negligible SQUID capacitance, the resonator's effective capacitance C_r and inductance L_r are [7]

$$C_r(x) = \frac{C_{\text{cav}}}{2} \left(1 + \frac{\sin(2x)}{2x} \right) \quad (\text{S2})$$

$$L_r(x) = \frac{L_{\text{cav}} C_{\text{cav}}}{x^2 C_r}, \quad (\text{S3})$$

where $x = k_n \ell$, and k_n is the eigenmode wave vector for the n th mode. The cavity capacitance and inductance are $C_{\text{cav}} = \mathcal{C} \ell$ and $L_{\text{cav}} = \mathcal{L} \ell$, respectively, where $\mathcal{C} = 173$ pF/m and $\mathcal{L} = 402$ nH/m are the capacitance and inductance per length for a 2:1 center:gap CPW on sapphire [8], respectively. The resonator frequency ω_r is

$$\omega_r(x) = \frac{x}{\sqrt{C_{\text{cav}} L_{\text{cav}}}}. \quad (\text{S4})$$

The energy deviation δE_n of the n th resonator level to first order from the linear resonator is [7]

$$\delta E_n(x) = \frac{-(6n^2 + 6n + 3)}{4} B_k E_C \quad (\text{S5})$$

$$B_k(x) = \frac{(1/4) \cos^2(x)}{1 + 2x/\sin(2x)}, \quad (\text{S6})$$

where $E_C = e^2/(2C_r)$. The anharmonicity α_r is then given by the deviation of the first and second levels from the ground and first level, noting that we need to convert energy to frequency via $\omega = E/\hbar$, as

$$\hbar \alpha_r = (\delta E_2 - \delta E_1) - (\delta E_1 - \delta E_0). \quad (\text{S7})$$

We plot the anharmonicity $\alpha_r/2\pi$ in Fig. S2. According to this model, throughout the full tuning range of the second eigenmode used for the experiments, the magnitude of the anharmonicity does not exceed 20 kHz, which is much less than both the resonator/qubit coupling (≈ 7 MHz) and the resonator/waveguide coupling (maximum ≈ 55 MHz).

Classical linear circuit model

We simulate the system with a simple linear model shown in Fig. S3a to help design parameters that allow us to turn the variable coupling on and off. This linear model is valid for small resonator anharmonicity and for weak coupling [9] and does not take into account losses in the circuit elements. The RF SQUID junction inductance is

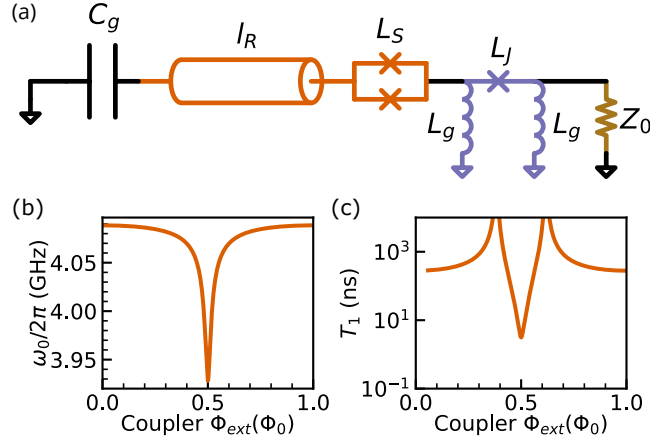


FIG. S3. (a) Linear circuit model of a tunable resonator coupled to a resistor. A small capacitance to ground $C_g = 10^{-14}$ F sets the boundary condition for a transmission line resonator (orange) of length $l_R = 20.5$ mm bounded at the other end by a SQUID with total inductance $L_S = 0.3$ nH. The resonator couples to a $Z_0 = 50 \Omega$ resistor through a variable coupler circuit (green) with inductance to ground $L_g = 0.2$ nH and variable single junction inductance $L_J(\Phi_{\text{ext}})$. (b) Resonant frequency for circuit model in (a) as a function of the external flux through the RF SQUID (variable coupler), see text for inductance to flux expression (c) Lifetime for circuit model in (a) as a function of the external flux through the RF SQUID. The minimum lifetime is $T_1 \approx 3$ ns.

related to the phase across the junction as $L_J = L_{j0}/\cos(\delta)$ with $L_{j0} = 0.6$ nH. The junction phase and external RF SQUID flux are related by [9]

$$\delta + \frac{L_l}{L_T} \sin(\delta) = 2\pi \frac{\Phi_{\text{ext}}}{\Phi_0}. \quad (\text{S8})$$

A resistance $Z_0 = 50 \Omega$ is used to model the dissipation load from an infinite transmission line with a characteristic impedance Z_0 [10]. Modeling the circuit as a parallel RLC resonator, we find the circuit resonance ω_p numerically when the imaginary part of the total circuit admittance $Y = 0$ as shown in Fig. S3b. The effective capacitance C_p of the resonator at the resonance is given by $C_p = (1/2)\text{Im}Y'(\omega_p)$ [11]. We then calculate the quality factor $Q_0 = \omega_p Z_0 C_p$ and the resonator lifetime $T_{1,r} = \omega_r/Q$ in Fig. S3c.

Quantum input-output wavepacket model

To simulate the release of a wavepacket by a resonator we use input-output theory with quantum pulses [12]. A wavepacket with normalized pulse shape $u(t)$ emitted by the tunable resonator is modeled as a virtual cavity with complex coupling to the tunable resonator

$$g_u(t) = \frac{u^*(t)}{\sqrt{1 - \int_0^t dt' |u(t')|^2}}, \quad (\text{S9})$$

while an incident pulse shape $v(t)$ couples with

$$g_v(t) = \frac{-v^*(t)}{\sqrt{\int_0^t dt' |v(t')|^2}}. \quad (\text{S10})$$

We model the wavepacket release and capture as separate processes, in the rotating frame of the (constant) tunable resonator frequency during the process. The total system Hamiltonian is given by [12]

$$\hat{H}(t) = \frac{i}{2} \left(\sqrt{\gamma(t)} g_u^*(t) \hat{a}_u^\dagger \hat{c} + \sqrt{\gamma^*(t)} g_v(t) \hat{c}^\dagger \hat{a}_v + g_u^*(t) g_v(t) \hat{a}_u^\dagger \hat{a}_v - \text{h.c.} \right), \quad (\text{S11})$$

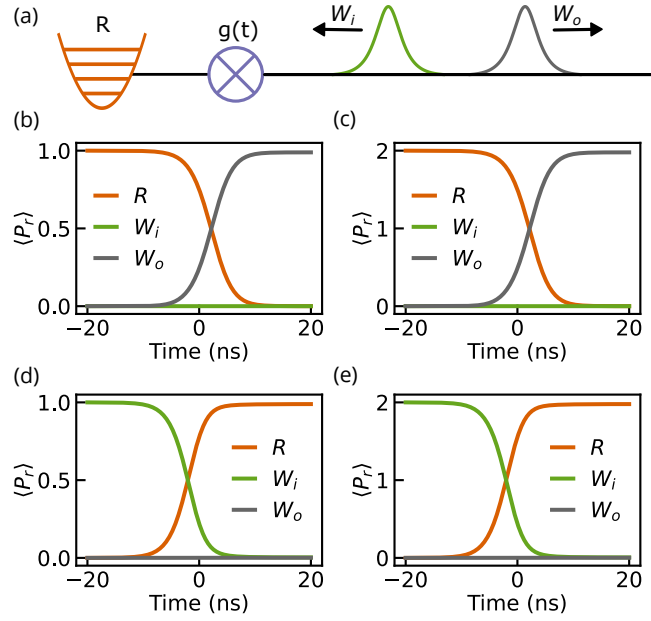


FIG. S4. (a) Schematic representing resonator R coupled to a waveguide through a variable coupling $g(t)$ with an incoming hyperbolic secant wavepacket W_i and outgoing wavepacket W_o . (b,c) Releasing 1 and 2 photons respectively from R into W_o with high efficiency (99% population transfer) using the same release parameters. (d,e) Capturing 1 and 2 photons respectively into R from W_i with high efficiency (99% population transfer) using the same capture parameters.

where $\gamma(t)$ is the time dependent resonator decay rate modulated by the variable coupler, \hat{c} is the lowering operator of the tunable resonator and $\hat{a}_u^\dagger = \int dt u(t)\hat{a}^\dagger(t)$ is the creation operator for the u virtual cavity with a similar expressions for v .

The Lindblad operator for the capture/emission process is

$$\hat{L}_0(t) = \sqrt{\gamma}\hat{c} + g_u(t)\hat{a}_u + g_v(t)\hat{a}_v. \quad (\text{S12})$$

Additional standard Lindblad operators are used to model the tunable resonator decay and dephasing. The Hamiltonian and Lindblad operators are then used to simulate the system dynamics with a QuTiP master equation solver [13].

Wavepacket release and capture

Using input-output formalism with quantum pulses [12] we simulate the release and capture of a single excitation with near unit transfer efficiency using a hyperbolic secant pulse shape, $u(t) \propto \text{sech}(\kappa_c t/2)$, where κ_c is the characteristic bandwidth of the wavepacket (Fig. S4b and c). The cavity energy relaxation to the waveguide $\kappa(t)$ that maximizes emission into this wavepacket is given by [14]

$$\kappa(t) = \kappa_m \frac{e^{\kappa_c(t-t_0)}}{1 + e^{\kappa_c(t-t_0)}}, \quad (\text{S13})$$

where κ_m the maximum coupling strength and t_0 varies the target output wavepacket in time. $\kappa(t)$ monotonically increases and then stays constant at its maximum value. We vary κ_m and t_0 to maximize population into the wavepacket[15]. In Fig. S4, $1/\kappa_c = 2 \text{ ns}$, $\kappa_m = 0.60 \text{ GHz}$, $t_0 = 2.62 \text{ ns}$, and have transfer efficiencies ≈ 0.99 . The discrepancy from unity efficiency is likely a numerical issue as the expression is analytically derived. Keeping all parameters constant in this numerical simulation except for the number of photons in the incoming pulse we capture the pulse with a similar efficiency. Similarly, it is possible in simulation to capture both single and multi-photon excitations from the sample wavepacket shape without changing experimental parameters after optimizing the single excitation catch.

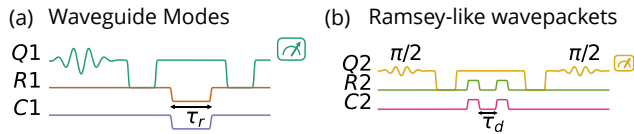


FIG. S5. Pulse sequences for Fig. 2 in the main text with qubits $Q1$ and $Q2$, resonators $R1$ and $R2$ and variable couplers $C1$ and $C2$. Microwave drives are depicted as oscillatory Gaussian pulses. The other shapes are applied fluxes through SQUIDS to tune component frequencies or coupling strength. Measured qubits are labeled with a measurement symbol at the end of sequences. (a) Waveguide modes seen from $R1$. After $Q1$ is excited, the excitation is swapped to $R1$, the coupler is turned on with weak coupling to the waveguide while the resonator frequency is shifted for time τ_r , the excitation is swapped back to $Q1$ and $Q1$ is measured. (b) Ramsey-like measurement of itinerant wavepackets. $Q2$ is prepared in a $|0\rangle + |1\rangle$ superposition which is swapped to $R2$. The excitation is released as a wavepacket with constant 20 ns rectangular pulses turning on the coupling while applying a flux through the resonator SQUID to change its frequency. After swapping back to $Q2$ a final $\pi/2$ pulse is applied before measurement.

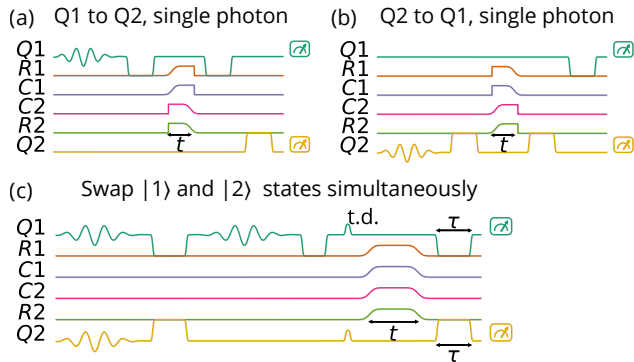


FIG. S6. Pulse sequences for Fig. 3 in the main text. (a) Single excitation transfer from $Q1$ to $Q2$. After exciting $Q1$, swap the excitation to $R1$, release the itinerant wavepacket from $R1$ and capture with $R2$, and swap population from both resonators to their respective qubits before measurement. (b) Similar to (a) in the opposite direction. (c) Simultaneous state swap between resonators. Excite both qubits and swap to respective resonators. $Q1$ is excited again and swapped into $R1$. A thermal dump t.d. resets the states of the qubits in preparation for tomography. The states from the both resonators are simultaneously released and after time t caught by the other resonator. Both qubits are tuned into resonance with the resonators for time τ and the qubit oscillations are fit to extract the resonator population distribution.

PULSE SEQUENCES

Pulse sequences for Fig. 2, 3, and 4 in the main text are shown in Fig. S5, Fig. S6, and Fig. S7 respectively.

DEVICE PARAMETERS

The qubit and readout parameters are given in table S1. The resonator and coupler parameters are given in table S2. The qubit state is measured via dispersive readout through a single stage asymmetric bandpass Purcell filter with inductively coupled input and output [16, 17].

Resonator Control

We prepare resonator states by resonantly swapping excitations using the frequency-tunable qubit [18–20]. With the resonator initially in the ground state, a qubit excitation transfers to the resonator in time $\tau_0 = \pi/2g_{qr}$, with $g_{qr}/2\pi = 6.8$ MHz the qubit/resonator coupling strength (Fig. S8a). For a resonator initially prepared in a higher excited state n this transfer time becomes shorter as $\tau_n = \tau_0/\sqrt{n}$. By repeatedly exciting and then swapping excitations from the qubit to the resonator, multi-photon resonator states are prepared. (Fig. S8b).

Fig. S8c-d further show how $|0\rangle + |N\rangle$ resonator superposition states are prepared using an ancilla qubit [21]. A

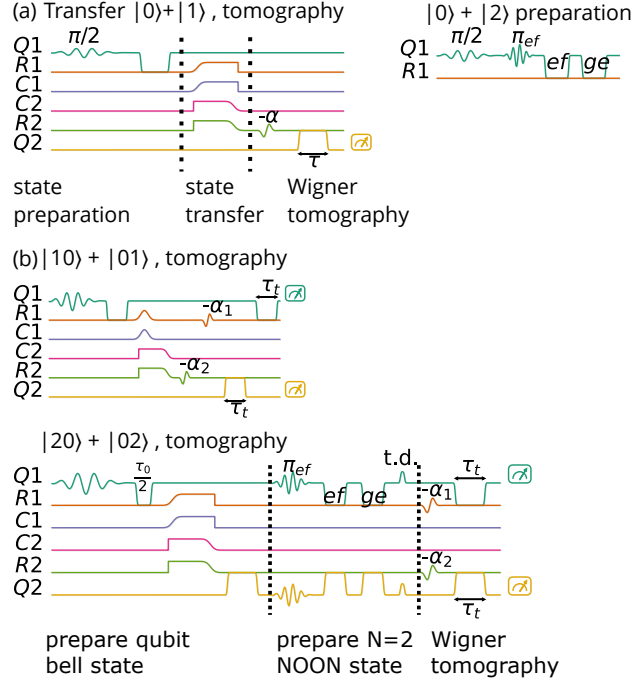


FIG. S7. Pulse sequences for Fig. 4 in the main text. (a) Prepare $|0\rangle + |1\rangle$ superposition state in $R1$, transfer the state, then displace $R2$ with a coherent pulse with amplitude $-\alpha$, then interact with qubit for time τ for Wigner tomography. The sequence for $|0\rangle + |2\rangle$ state preparation for $R2$ is shown and state transfer and Wigner tomography is otherwise identical to the $|0\rangle + |1\rangle$ sequence. (b) Fig. 3b, Create an entangled resonator Bell state $|10\rangle + |01\rangle$ by swapping a full excitation from $Q1$ to $R1$, releasing half the resonator state into the waveguide as a shaped wavepacket and capturing at $R2$, then measure resonators with joint Wigner tomography. For the $|20\rangle + |02\rangle$ state we first create an entangle qubit Bell state by swapping half of a full excitation from $Q1$ to $R1$, transferring the resonator state, and then swapping the state from $R2$ to $Q2$. The $N = 2$ NOON state is created by driving the ef qubit transition on both qubits, then swapping the qubit state to the resonator. We finally measure both resonators with joint Wigner tomography.

$|0\rangle + |1\rangle$ resonator state is made by resonantly interacting the qubit in state $|g\rangle + |e\rangle$ with the resonator initially in the ground state for time τ_0 . To prepare larger $|0\rangle + |N\rangle$ resonator states we first excite the transmon from $|g\rangle + |e\rangle$ to $|g\rangle + |f\rangle$, and then swap the highest qubit excitation into the resonator. If $N = 2$, we swap the remaining qubit excitation into the resonator (Fig. S8d). Otherwise, for higher N we excite the $|e\rangle - |f\rangle$ transition and swap to the resonator for the additional excitations.

DEVICE CHARACTERIZATION

Qubit/Resonator coupling

Fig. S9a shows the $Q1/R1$ two-tone spectroscopy [22] avoided level crossing with coupling strength 6.8 MHz.

Resonator characterization

In Fig. S10 $R1$ is tuned to both maximum and minimum coupling to the waveguide, demonstrating a wide range of control for the wavepacket emission. With the coupling to the waveguide off, Fig. S11 shows both resonator lifetimes as a function of the resonator frequencies. Around 4 GHz, both resonator lifetimes are above $1 \mu\text{s}$ which is suitable for our experiments. Above 4.2 GHz is a sharp decrease in the resonator lifetimes, possibly a box mode due to the large chip package. The reduction in the T_1 for $R1$ has been seen with similar tunable resonator designs[24].

Qubit parameters	Qubit 1	Qubit 2
Qubit bare frequency, $\omega_{qb}/2\pi$	6.250 GHz	6.242 GHz
Qubit capacitance, C_q (design value)	90 fF	90 fF
Qubit anharmonicity α_q	-192 MHz	-192 MHz
Qubit lifetime, T_{1q}	20 μ s	22 μ s
Qubit Ramsey dephasing time, $T_{2q,\text{Ramsey}}$	2.62 μ s	0.56 μ s
Qubit spin-echo dephasing time, T_{2E} (μ s)	4.20 μ s	3.95 μ s
$ e\rangle$ state readout fidelity, F_e	0.95	0.96
$ g\rangle$ state readout fidelity, F_g	0.98	0.97
Thermal excited state population	0.010	0.026
Readout resonator frequency, $\omega_{ro}/2\pi$	5.358 GHz	5.312 GHz
Readout resonator decay rate (design value), $\kappa_r/2\pi$	4.58 MHz	4.58 MHz
Readout dispersive shift, $\chi/2\pi$	1.4 MHz	1.3 MHz

Purcell filter parameters	value
Input quality factor (design value), Q_{fi}	~ 2000
Output quality factor (design value), Q_{fo}	15.5
Purcell filter frequency (design value), $\omega_p/2\pi$	5.29 GHz

TABLE S1. Qubit and readout parameters.

Variable resonator parameters	Resonator 1	Resonator 2
Qubit/resonator coupling, $g_{qr}/2\pi$	6.805 MHz	6.830 MHz
Resonator lifetime (4.058 GHz), T_{1r}	4.57 μ s	0.86 μ s
Resonator Ramsey dephasing time (4.058 GHz), $T_{2r,\text{Ramsey}}$	0.95 μ s	0.90 μ s
Resonator bare frequency $\omega_r/2\pi$	4.269 GHz	4.269 GHz
Resonator DC SQUID inductance (design value), L_{rs}	0.25 nH	0.25 nH

Variable coupler parameters	Coupler 1	Coupler 2
Coupler junction inductance (design value) L_{cj}	0.6 nH	0.6 nH
Coupler grounding inductance, L_g (design value)	0.2 nH	0.2 nH
Coupler stray inductance, L_g (assumed design value)	0.1 nH	0.1 nH

TABLE S2. Resonator and coupler parameters.

Waveguide Characterization

We swap single excitations into single waveguide standing modes with frequencies across several hundred MHz to characterize their loss as shown in Fig. S12. The standing mode loss measurements strongly suggests that waveguide loss is not the dominant source of infidelity in the experiment.

Wavepacket Characterization

Before optimizing the release and capture of the wavepackets, we roughly estimate the wavepacket shape by applying a flattop pulse (Gaussian convolved with rectangular pulse) with varying rise times w and then monitor the resonator population as a function of time while strongly coupled to the waveguide, as shown in Fig. S13a. This is not in general an optimized coupling shape, however it gives us a sense of the range of wavepacket shapes we can generate. If the coupling to the waveguide is ramped up quickly, then the release is dominated by an exponential decay and lead to an asymmetric curve. For slow Gaussian ramp up the asymmetry is in the opposite direction. We characterize this asymmetry by modeling the wavepacket as a skewed hyperbolic secant $f(t, \theta, w)$ with skew θ and width w .

$$f(t) = \cos \theta \frac{e^{\frac{\theta(t-t_0)}{w}}}{2 \cosh\left(\frac{\pi(t-t_0)}{2w}\right)}. \quad (\text{S14})$$

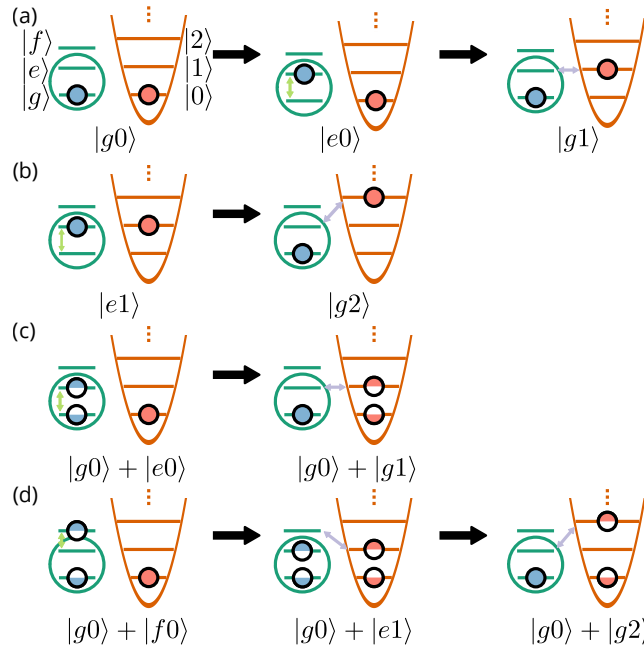


FIG. S8. Resonator Fock and superposition state preparation (a) Steps to prepare a single photon state by swapping excitations from a transmon qubit. The qubit is depicted on the left (blue) and resonator on the right (red). Both systems are initially prepared in their respective ground states. The qubit is excited to $|e\rangle$, and then that excitation is swapped into the resonator in time τ_{swap} with both systems on resonance. (b) A two-photon state in the resonator is prepared by starting with the single photon state in (a), exciting the qubit, then swapping the excitation to the resonator in time $\tau_{\text{swap}}/\sqrt{2}$. (c) A resonator $|0\rangle + |1\rangle$ state is prepared by first preparing $|g\rangle + |e\rangle$ in the qubit, then swapping the excited state to the resonator. (d) A resonator $|0\rangle + |2\rangle$ is prepared by starting from the qubit $|g\rangle + |e\rangle$ state (first step in (c)) then exciting the qubit to $|g\rangle + |f\rangle$. Two swaps into the resonator (both $\tau_{\text{swap}}/\sqrt{2}$) then creates a $|0\rangle + |2\rangle$ resonator state.

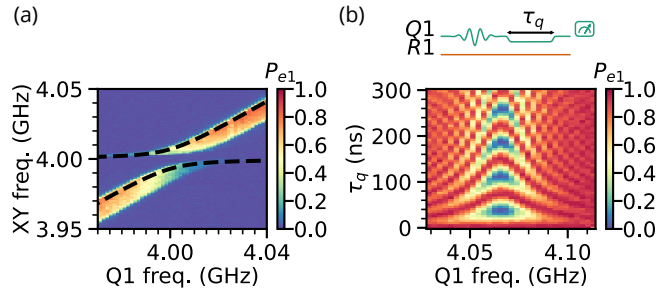


FIG. S9. (a) Q1 two-tone spectroscopy showing avoided level crossing with R1. The peak is broadened, likely due to pulse distortion in the qubit flux bias. We fit the avoided level crossing by eye to be approximately $g/2\pi \approx 7$ MHz. (c) After correcting for pulse distortion [23], the qubit/resonator swaps show the characteristic chevron shape with $g/2\pi = 6.8$ MHz.

The exponential adds a skew to a hyperbolic secant function, and the cosine normalizes the integral of the function to one. This function is not derived from the experimental circuit, it simply happens to fit the data reasonably well and lets us extract the skew of the wavepacket from a fit. Ideally, the skew should be zero for a time-symmetric wavepacket. Fitting the wavepackets with this function as shown in Fig. S13b, we find wavepackets with varying asymmetries. This is only a rough estimate for the wavepacket shape as the time to turn off the coupling is finite and so distorts the measured pulse shape.

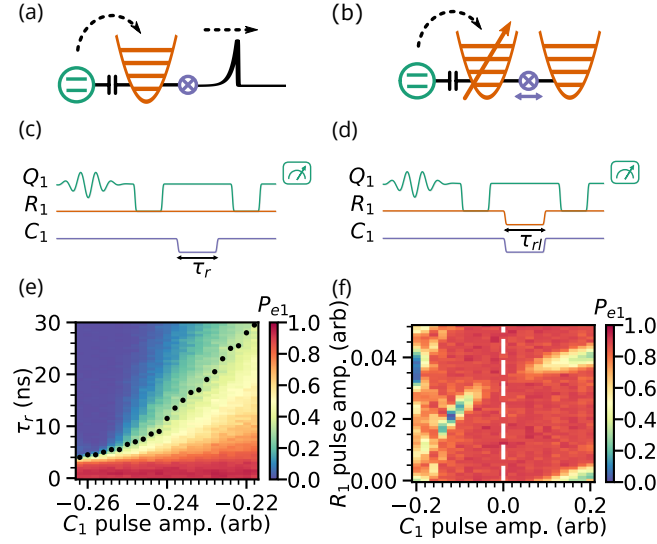


FIG. S10. Cartoon (a), pulse sequence (c), and data (e) of a single excitation decaying from $R1$ into the waveguide. $R1$ is coupled to the waveguide with varied coupling strength controlled by $C1$, for time $\tau_r < 30$ ns before reflections returning from the far end of the waveguide are visible. Black dots show when $R1$ population is $1/e$ the value at 0 ns, showing that population is released into the waveguide with characteristic time under 4 ns. Cartoon (b), pulse sequence (d), and data (f) for method to find zero coupling point between the resonator and waveguide, shown as a dotted line in (f). After swapping a single excitation into the resonator we set the delay time $\tau_{rl} = 200$ ns and then vary the $C1$ coupling strength until the $R1$ population is independent of frequency.

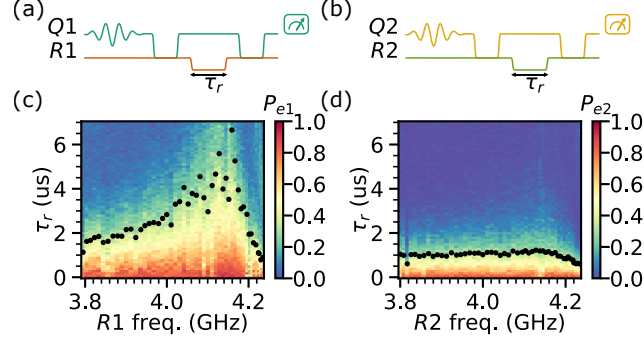


FIG. S11. Pulse sequence (a) and data (b) for T_1 measurement of $R1$ as a function of its frequency. Black dots are fits to exponential decay. A sharp decrease in lifetime above 4.2 GHz possibly a box or chip mode interacting with the resonator. (c) T_1 measurement of $R2$. T_1 is flat with frequency below 4.2 GHz (with a similar drop as in (a) above 4.2 GHz and similar shape at long delay τ_r). This may indicate that the resonator's DC SQUID is not the dominant loss channel.

STATE TRANSFER

Single excitation transfer, Swaps

We also transfer energy between resonators by swapping into a single waveguide mode. After exciting qubit 1, swapping into resonator 1, a single waveguide mode at 4.157 GHz, resonator 2 and finally qubit 2, we measure around 0.78 population in the second qubit. Numerical simulations of this transfer that include a 94% visibility, and qubit/resonator decay and dephasing predict a 0.84 population in qubit 2 for the same process. The rest of the discrepancy may be due to incomplete energy transfer between components.

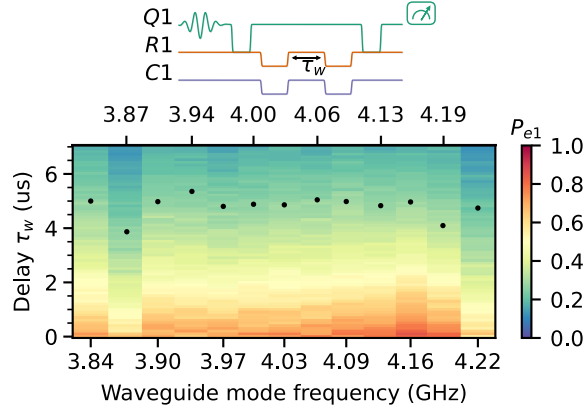


FIG. S12. Waveguide mode T_1 measurement. A one photon excitation from $Q1$ is swapped first into $R1$ and then into a waveguide mode. After waiting variable time τ_w , the excitation is swapped back to $R1$ and then to $Q1$.

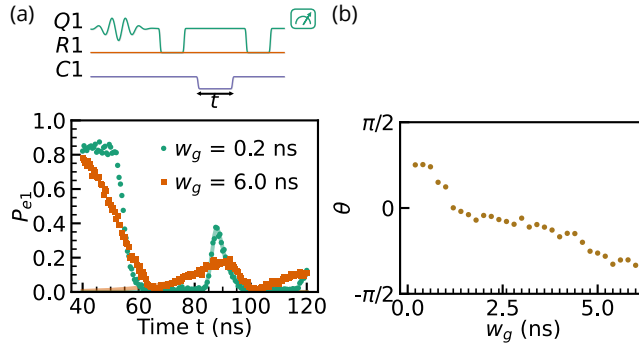


FIG. S13. (a) Releasing a wavepacket with a flattop pulse of varying Gaussian rise widths w_g . The wavepacket bounces off the other end of the waveguide and we measure the resonator population with the coupler fully on. The wavepackets are then fit to a skewed hyperbolic secant with skew θ shown in (b), excluding the data points from release and second reflection. (b) Varying w_g and fitting the wavepackets we see a decreasing trend between w_g and θ .

Single excitation transfer, wavepacket

We optimize the release and capture pulses for single excitations by maximizing population transfer, and then use the same parameters for general resonator state transfer. Gaussian filters in our wiring smooth arbitrarily generated pulses on the order of 3 ns limiting the time resolution for pulse control and making it difficult to reproduce analytic pulse shapes and timing for optimal state transfer as in Ref. [14]. Here we use a Bayesian optimization package to vary the pulse shape in the time domain for release and capture [25], maximizing the total transferred amplitude from an initial single excitation in the releasing resonator. This optimization for wavepacket release and capture is done independently for both transfer directions.

Wigner tomography

The Wigner function $W(\alpha)$ is a quasiprobability distribution for a resonator's quantum state which can be calculated from the density matrix ρ [26]

$$W(\alpha) = \frac{2}{\pi} \text{Tr} [D(-\alpha)\rho D(\alpha)\mathcal{P}], \quad (\text{S15})$$

where Tr is the trace, $D(-\alpha) = D^\dagger(\alpha) = \exp(\alpha^*a - \alpha a^\dagger)$ is the displacement operator for the resonator, \mathcal{P} is the resonator's photon number parity, and $\alpha = x + ip$ is the complex phase space coordinate. x and p are the

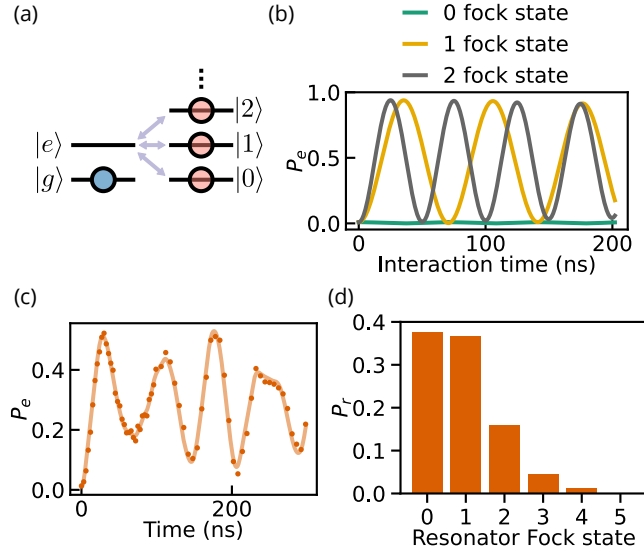


FIG. S14. (a) A resonator with unknown state couples to a qubit prepared in the ground state (b) Simulation for qubit/resonator oscillations with the resonator prepared in single Fock states. The qubit oscillates τ_0/\sqrt{n} , where τ_0 is the period for a single excitation (c) For an arbitrary resonator state, the qubit population over time is the linear combination of the oscillations that would occur for each prepared Fock state as in (b). Data (points) and fit to model (line) are shown (d) Resonator occupation probability distribution from fitting the data in (c). We see that the resonator has a Fock distribution consistent with a coherent state with $\alpha \approx 1$.

resonator's position and momentum variables respectively. Applying the displacement operator on the resonator ground state $|0\rangle$ creates coherent states $|\alpha\rangle$. Experimentally, α is also the coherent displacement of the resonator with $-\alpha = (\frac{1}{2}) \int \Omega_r(t) dt$, where Ω_r is a complex drive amplitude [20].

We displace the resonator by capacitively coupling a signal line to the resonator. The Fock state probability distribution is measured by resonantly interacting the qubit with the resonator and fitting the oscillations to a system model[18, 20, 21], as shown in Fig. S14. The resonator parity is then calculated from that distribution.

If the resonator is prepared in a well-defined Fock state, then a qubit prepared in the ground state goes through Rabi oscillations with a period of τ_0/\sqrt{n} , where τ_0 is the period for a single excitation. If the resonator is prepared with a superposition of Fock states, the qubit oscillates following a linear combination of these oscillations proportional to their associated resonator populations.

To reconstruct the density matrix from the Wigner function we use a MATLAB package [27] that uses convex optimization to find the most likely ρ given the measured photon number distributions as a function of displacement [28]. During this reconstruction procedure we constrain ρ to be Hermitian, positive semi-definite, and have a trace equal to 1. The joint resonator density matrix reconstruction for NOON states further constrain elements with photon indices larger than N to zero [21].

Microwave displacement calibration and crosstalk

Using the resonant photon state reconstruction technique we calibrate the resonator displacement pulses. Fig. S16a shows the average photon number after applying a 20 ns displacement pulse and fitting the qubit/resonator interaction. Displacement amplitude $\propto V$ (proportional to V), and since the photon number $n \propto V^2$, $n \propto$ the square of the displacement amplitude. At higher photon numbers the linear relationship deviates, possibly due to either resonator nonlinearity or photon number fitting errors. For a coherent state $\langle n_\alpha \rangle = |\alpha|^2$, so the slope of this line gives the calibration factor between α and the displacement amplitude, in the case of Fig. S16a, the slope is 3.44.

Microwave crosstalk occurs when we want to only apply a microwave tone to one component but affect other components as well. This may occur because of unintended coupling in either the microwave lines or sample packaging. In our system the two qubits are detuned from each other by tens of MHz so that microwave crosstalk between the two is minimal. This is confirmed by separately exciting the two qubits and jointly measuring them to monitor the ground state populations. The tunable resonators are detuned from the qubits by several hundred MHz when applying

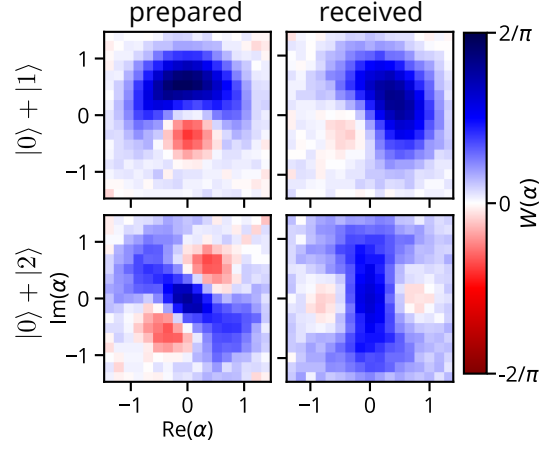


FIG. S15. Wigner tomograms using resonator parity data for Fig. 2a in the main text.

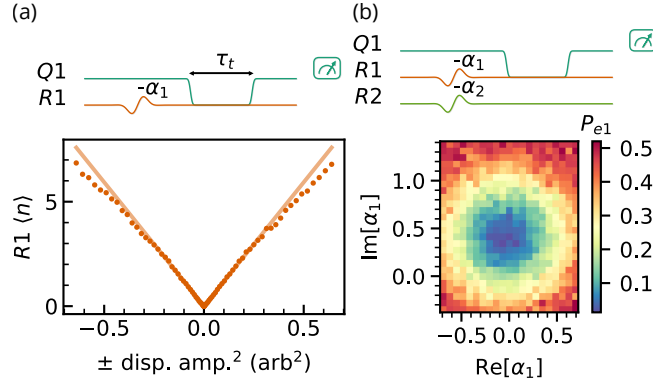


FIG. S16. (a) Calibration measurement for α . We displace the resonator and measure the average population of the resonator. Fitting the time trace with a qubit/resonator model returns a linear relationship at low photon powers with the square of the displacement amplitude. The linear fit here is up to 0.4 displacement amplitude which roughly corresponds to $n \approx 1.9$. (b) Microwave crosstalk node 2 on node 1. We apply a constant displacement pulse min α_2 with $R2$'s displacement line that would correspond to a photon population in $R2$ of $\langle n_2 \rangle \approx 2.7$. At the same time we apply a displacement α_1 on resonator 1, and then swap the resulting population into $Q1$ at the 1 photon swap time $\tau_0 = 38$ ns. When α_1 cancels the crosstalk from the displacement from node 2 we measure 0 population in $Q1$.

microwave pulses, and so have negligible microwave crosstalk between the two. However, the tunable resonators are at the same frequency, and so there is non-negligible crosstalk between them. When we apply a microwave pulse to displace resonator 1 with amplitude a_1 and phase θ_1 , we also displace resonator 2 with amplitude a_{12} and phase θ_{12} . Similarly there is crosstalk in the other direction. We correct for this crosstalk when we need to simultaneously measure the state of both resonators, as in the NOON state experiments.

To measure this crosstalk we use a similar procedure that we use for calibrating displacement amplitude to resonator α for a single resonator: Wigner tomography with the resonator prepared in the ground state, and scanning the displacement amplitude. However, instead of displacing the resonator using its own displacement line, we use the microwave crosstalk from the other resonator displacement line. We measure the phase of this crosstalk relative to the 0 phase for each resonator, by applying displacements from both displacement lines and measuring at which phase the two tones cancel each other as in Fig. S16b. This crosstalk is quite large, when applying a displacement pulse $-\alpha_2$ to populate resonator 2 with 1 photon we also populate resonator 1 with 0.07 photons. We correct for microwave crosstalk when processing the data.

Flux crosstalk is corrected for qubits and couplers by applying corrective pulses in the experiment.

-
- [1] J. S. Kelly, *Fault-tolerant superconducting qubits*, Ph.D. thesis, University of California, Santa Barbara (2015).
- [2] A. Dunsworth, A. Megrant, C. Quintana, Z. Chen, R. Barends, B. Burkett, B. Foxen, Y. Chen, B. Chiaro, A. Fowler, R. Graff, E. Jeffrey, J. Kelly, E. Lucero, J. Y. Mutus, M. Neeley, C. Neill, P. Roushan, D. Sank, A. Vainsencher, J. Wenner, T. C. White, and J. M. Martinis, Characterization and reduction of capacitive loss induced by sub-micron Josephson junction fabrication in superconducting qubits, *Applied Physics Letters* **111**, 022601 (2017), <https://doi.org/10.1063/1.4993577>.
- [3] A. Dunsworth, R. Barends, Y. Chen, Z. Chen, B. Chiaro, A. Fowler, B. Foxen, E. Jeffrey, J. Kelly, P. V. Klimov, E. Lucero, J. Y. Mutus, M. Neeley, C. Neill, C. Quintana, P. Roushan, D. Sank, A. Vainsencher, J. Wenner, T. C. White, H. Neven, J. M. Martinis, and A. Megrant, A method for building low loss multi-layer wiring for superconducting microwave devices, *Applied Physics Letters* **112**, 063502 (2018), <https://doi.org/10.1063/1.5014033>.
- [4] J. Grebel, *Bidirectional multi-photon communication between remote superconducting resonators*, Ph.D. thesis, The University of Chicago (2023).
- [5] S. Huang, B. Lienhard, G. Calusine, A. Vepsäläinen, J. Braumüller, D. K. Kim, A. J. Melville, B. M. Niedzielski, J. L. Yoder, B. Kannan, T. P. Orlando, S. Gustavsson, and W. D. Oliver, Microwave package design for superconducting quantum processors, *PRX Quantum* **2**, 020306 (2021).
- [6] M. Esposito, A. Ranadive, L. Planat, and N. Roch, Perspective on traveling wave microwave parametric amplifiers, *Appl. Phys. Lett.* **119**, 120501 (2021).
- [7] M. Wallquist, V. S. Shumeiko, and G. Wendin, Selective coupling of superconducting charge qubits mediated by a tunable stripline cavity, *Phys. Rev. B* **74**, 224506 (2006).
- [8] Y. Zhong, *Violating Bell's inequality with remotely-connected superconducting qubits*, Ph.D. thesis, The University of Chicago (2019).
- [9] M. R. Geller, E. Donate, Y. Chen, M. T. Fang, N. Leung, C. Neill, P. Roushan, and J. M. Martinis, Tunable coupler for superconducting Xmon qubits: Perturbative nonlinear model, *Phys. Rev. A* **92**, 012320 (2015).
- [10] D. M. Pozar, *Microwave engineering* (John Wiley & Sons, 2009).
- [11] S. E. Nigg, H. Paik, B. Vlastakis, G. Kirchmair, S. Shankar, L. Frunzio, M. H. Devoret, R. J. Schoelkopf, and S. M. Girvin, Black-box superconducting circuit quantization, *Phys. Rev. Lett.* **108**, 240502 (2012).
- [12] A. H. Küllerich and K. Mølmer, Input-output theory with quantum pulses, *Phys. Rev. Lett.* **123**, 123604 (2019).
- [13] J. R. Johansson, P. D. Nation, and F. Nori, Qutip: An open-source python framework for the dynamics of open quantum systems, *Computer Physics Communications* **183**, 1760 (2012).
- [14] A. Bienfait, K. J. Satzinger, Y. P. Zhong, H.-S. Chang, M.-H. Chou, C. R. Conner, É. Dumur, J. Grebel, G. A. Peairs, R. G. Povey, and A. N. Cleland, Phonon-mediated quantum state transfer and remote qubit entanglement, *Science* **364**, 368 (2019), <https://science.sciencemag.org/content/364/6438/368.full.pdf>.
- [15] If we vary t_0 away from release window, the resonator would still decay as expected, but there would not be any excitations contained in the time envelope for the wavepacket shape we defined.
- [16] D. T. Sank, *Fast, Accurate State Measurement in Superconducting Qubits*, Ph.D. thesis.
- [17] H. Yan, X. Wu, A. Lingenfelter, Y. J. Joshi, G. Andersson, C. R. Conner, M.-H. Chou, J. Grebel, J. M. Miller, R. G. Povey, *et al.*, Broadband bandpass purcell filter for circuit quantum electrodynamics, .
- [18] Y. xi Liu, L. F. Wei, and F. Nori, Generation of nonclassical photon states using a superconducting qubit in a microcavity, *Europhysics Letters* **67**, 941 (2004).
- [19] M. Hofheinz, E. M. Weig, M. Ansmann, R. C. Bialczak, E. Lucero, M. Neeley, A. D. O'Connell, H. Wang, J. M. Martinis, and A. N. Cleland, Generation of Fock states in a superconducting quantum circuit, *Nature* **454**, 310 (2008).
- [20] M. Hofheinz, H. Wang, M. Ansmann, R. C. Bialczak, E. Lucero, M. Neeley, A. D. O'Connell, D. Sank, J. Wenner, J. M. Martinis, and A. N. Cleland, Synthesizing arbitrary quantum states in a superconducting resonator, *Nature* **459**, 546 (2009).
- [21] H. Wang, M. Mariantoni, R. C. Bialczak, M. Lenander, E. Lucero, M. Neeley, A. D. O'Connell, D. Sank, M. Weides, J. Wenner, T. Yamamoto, Y. Yin, J. Zhao, J. M. Martinis, and A. N. Cleland, Deterministic entanglement of photons in two superconducting microwave resonators, *Phys. Rev. Lett.* **106**, 060401 (2011).
- [22] A. Wallraff, D. I. Schuster, A. Blais, J. M. Gambetta, J. Schreier, L. Frunzio, M. H. Devoret, S. M. Girvin, and R. J. Schoelkopf, Sideband transitions and two-tone spectroscopy of a superconducting qubit strongly coupled to an on-chip cavity, *Phys. Rev. Lett.* **99**, 050501 (2007).
- [23] Z. Chen, *Metrology of quantum control and measurement in superconducting qubits*, Ph.D. thesis, University of California, Santa Barbara (2018).
- [24] Z. L. Wang, Y. P. Zhong, L. J. He, H. Wang, J. M. Martinis, A. N. Cleland, and Q. W. Xie, Quantum state characterization of a fast tunable superconducting resonator, *Applied Physics Letters* **102**, 163503 (2013), <https://doi.org/10.1063/1.4802893>.
- [25] F. Nogueira, Bayesian Optimization: Open source constrained global optimization tool for Python (2014-).
- [26] S. Haroche and J.-M. Raimond, *Exploring the quantum: atoms, cavities, and photons* (Oxford university press, 2006).
- [27] M. Grant and S. Boyd, CVX: Matlab software for disciplined convex programming, version 2.1, <http://cvxr.com/cvx> (2014).
- [28] I. Strandberg, Simple, reliable, and noise-resilient continuous-variable quantum state tomography with convex optimization, *Phys. Rev. Appl.* **18**, 044041 (2022).